Macroscopic quasilinear theory of parallel electron firehose instability associated with solar wind electrons

M. Sarfraz, P. H. Yoon, Sundas Saeed, G. Abbas, and H. A. Shah

Citation: Phys. Plasmas **24**, 012907 (2017); doi: 10.1063/1.4975007
View online: http://dx.doi.org/10.1063/1.4975007
View Table of Contents: http://aip.scitation.org/toc/php/24/1
Published by the American Institute of Physics

Macroscopic quasilinear theory of parallel electron firehose instability associated with solar wind electrons

M. Sarfraz,[1,2] P. H. Yoon,[2,3] Sundas Saeed,[1,2] G. Abbas,[1] and H. A. Shah[4,a)]
[1]*Department of Physics, GC University Lahore, Katchery Road, Lahore 54000, Pakistan*
[2]*Institute for Physical Science and Technology, University of Maryland, College Park, Maryland 20742, USA*
[3]*School of Space Research, Kyung Hee University, Yongin, South Korea*
[4]*GC University Lahore, Katchery Road, Lahore 54000, Pakistans*

(Received 2 November 2016; accepted 6 January 2017; published online 27 January 2017)

A number of different microinstabilities are known to be responsible for regulating the upper bound of temperature anisotropies in solar wind protons, alpha particles, and electrons. In the present paper, quasilinear kinetic theory is employed to investigate the time variation in electron temperature anisotropies in response to the excitation of parallel electron firehose instability in homogeneous and non-collisional solar wind plasma under the condition of $T_{\|e} > T_{\perp e}$. By assuming the bi-Maxwellian form of velocity distribution functions, various velocity moments of the particle kinetic equation are taken in order to reduce the theory to macroscopic model in which the wave-particle interaction is incorporated, hence, the *macroscopic* quasilinear theory. The threshold condition for the parallel electron firehose instability, empirically constructed as a curve in $(\beta_{\|e}, T_{\perp e}/T_{\|e})$ phase space, is implicit in the present macroscopic quasilinear calculation. Even though the present calculation excludes the oblique firehose instability, which is known to possess a higher growth rate, the basic methodology may be further extended to include such a mode. Among the findings is that the parallel electron firehose instability dynamically couples the electrons and protons, which implies that this instability may be important for overall solar wind dynamics. The present analysis shows that the macroscopic quasilinear approach may eventually be incorporated in global-kinetic models of the solar wind electrons and ions. *Published by AIP Publishing.* [http://dx.doi.org/10.1063/1.4975007]

I. INTRODUCTION

The study of radially expanding solar wind along with the mechanism of energy flow and dissipation within remain a subject of interest for many years.[1–4] In collisionless and magnetized plasmas, the transport of electron thermal and suprathermal energy is important for solar wind[5] and also for different astrophysical contexts including stellar winds and cooling flows in clusters of galaxies.[6] Marsch[7] studied the role of Coulomb collisional transport and wave-particle interaction in a combined manner for determining the solar wind electron dynamics. He further suggested to investigate the individual contributions of the above-mentioned processes for thermal conduction in interplanetary medium. Scime *et al.*[8] employed the Ulysses data[9] and emphasized the role of plasma instabilities in heat flux regulation instead of collision and its free expansion along the magnetic field. The literature is abundant with linear theories for plasma instabilities in the solar wind.[10–12]

Manheimer and Boris[13] proposed a simple approach to relate the microphysics of collisionless instabilities to plasma macro-physics. The underlying idea of the approach has two main points. (1) For a stable system, no enhanced fluctuations are observed, and there will be no limits on macroscopic parameters of plasma. (2) In contrast, if the system dynamics leads to an unstable state, then the enhanced fluctuations will appear leading to wave-particle scattering, which in turn, rapidly put constraints on this unstable state and take the plasma to a condition of instability threshold. The same approach was successfully applied to discuss the proton temperature anisotropies and whistler heat flux instability in terrestrial magnetosheath and solar wind.[14,15] Specifically, Gary *et al.*[15] suggested to adopt the principles and method of this approach for any collisionless and homogeneous plasma, which excites one or more plasma instabilities.

Of the electron anisotropy-driven instabilities, the electron firehose (EFH) instability plays an important role in solar flares and solar wind to regulate the parallel upper bound of electron temperature anisotropy. Electron firehose instability was first discussed by the linear theory assuming a parallel propagation with respect to the ambient magnetic field vector.[16–20] Many authors analyzed this unstable mode along with its marginal stability condition with the aid of solution of linearized Vlasov theory, simulations, or by fitting observations. In a bi-Maxwellian plasma, Hollweg[21] analyzed the growth rate of EFH instability. Later, the investigation was extended for non-Maxwellian plasmas.[22] Moreover, an interplay of EFH instability with Weibel instability (WI)[23] and with ordinary-mode instability[24] has also been discussed. The left-handed (LH) circularly polarized parallel propagating mode is excited for a plasma system that is hotter in the direction of a static magnetic field (i.e., $T_{\|e} > T_{\perp e}$). In general, the linearized Vlasov theory is encapsulated in the correlation between the electron temperature ratio, $T_{\perp e}/T_{\|e}$, and parallel plasma beta, $\beta_{\|e}$, as[24]

$$\frac{T_{\perp e}}{T_{\|e}} = 1 - \frac{S}{\beta_{\|e}^{\alpha}}, \tag{1}$$

a)Electronic mail: yoonp@umd.edu

where S and α are the fitting parameters.

Obliquely-propagating electron firehose instability was also discovered and discussed in terms of linear theory.[25,26] In general, the growth rate associated with the oblique mode is higher than that of the parallel electron firehose instability. Simulation of parallel electron firehose instability was performed by Ref. 27, and subsequently, more general simulations of oblique electron firehose instability were carried out for one-dimensional and two-dimensional situations by Refs. 28–30. Note that Gary and Nishimura's simulation is one dimensional, but their simulation considered magnetic field vector oriented at highly oblique angles with respect to the simulation axis.

In spite of these developments, quasilinear analysis of either parallel or oblique firehose instability has not been carried out in the literature. The aim of the present paper is to go beyond the linear theory and solve the quasilinear kinetic equations for parallel electron firehose instability as a first step. In the present analysis, we make a simplifying assumption of bi-Maxwellian form of particle velocity distribution functions such that instead of solving the particle kinetic equations directly, we take the velocity moments of the equation so that the problem reduces to a set of evolution equations for macroscopic quantities, i.e., perpendicular and parallel temperatures, but unlike the customary fluid approach, the influence of wave-particle dynamics is incorporated through the wave kinetic equation. Such an approach may be termed the *macroscopic* quasilinear theory for obvious reasons.

In view of the fact that particle-in-cell simulation works are already available in the literature,[27–30] it may be natural to question the value of quasilinear analysis, since the simulations are more rigorous. However, simulations require large computational resources, and it is not so straightforward to incorporate such approaches in large scale systems. In contrast, the macroscopic quasilinear theory can easily be incorporated into global kinetic models of the solar wind, for instance, of the type developed for protons by Ref. 31. For this reason, we believe that the quasilinear theory has its value, and its validity should be explored by comparison against simulations, e.g.,[32–35] As a first step, the present paper presents the quasilinear analysis of parallel electron firehose instability. More general quasilinear analysis for oblique electron firehose instability can and should be done, but such a task is beyond the scope of the present paper.

A corollary of the approach taken in the present paper is that the inverse correlations of parallel EFH instability of the type given by Eq. (1) is automatically built into the macroscopic quasilinear theory, by virtue of the assumption of bi-Maxwellian distribution. As such, the saturation stage naturally corresponds to the empirical marginal stability curve. The present approach, however, contains more information than simply the inverse relationship, since the time scale of the saturation stage as well as the asymptotic wave energy density cannot be estimated on the basis of linear theory. A similar methodology has already been adopted successfully for proton anisotropy driven instabilities for homogeneous,[36,37] spatially inhomogeneous,[31] and temporally varying magnetic field and density.[38] Note that the idea of incorporating the temperature anisotropy inverse relationships to macroscopic model have been entertained by Denton *et al.*[39] and Hellinger and Trávníček.[40] Chandran *et al.*[41] actually incorporated such a relationship as a form of closure relationship in the solar wind model for the first time. Yoon and Seough,[31] on the other hand, made use of much simpler models for the background quantities when compared with Ref. 41, but instead, they focused on a more self-consistent wave-particle dynamics. The present paper is not immediately involved with macro-kinetic modeling efforts as briefly overviewed above, but rather, the purpose of the present investigation is to lay down the foundation for future such works.

The structure of the present paper is as follows: In Section II, we will briefly discuss the linear and quasilinear theory of electron fire hose instability. Section III will present the numerical solutions. A brief summary and discussion are given in Section IV.

II. THEORETICAL FORMALISM

Strictly parallel (or antiparallel) to the stationary magnetic field, the electromagnetic modes are not only decoupled from the electrostatic oscillations, but also in some cases, manifest maximum growth rates, even though in the case of electron firehose instabilities, it is known that obliquely propagating modes possess a higher growth rate. Nevertheless, for the sake of simplicity, we presently consider the parallel propagation. Among many works, Refs. 12 and 42, as representative references, simplified the general (non-relativistic) dispersion relation for these parallel propagating modes as given

$$\frac{c^2k^2}{\omega^2} = 1 + \sum_{a=i,e} \frac{\omega_{pa}^2}{\omega^2} \int d\mathbf{v}\, \frac{v_\perp/2}{\omega - kv_\parallel \pm \Omega_a} \times \left((\omega - kv_\parallel) \frac{\partial f_a}{\partial v_\perp} + kv_\perp \frac{\partial f_a}{\partial v_\parallel} \right). \tag{2}$$

where $v_\perp$ and $v_\parallel$ are components of velocity perpendicular and parallel to the external magnetic field, respectively; ω and k are the angular frequency and wave number of the wave, respectively; $\omega_{pa} = (4\pi n_0 e^2/m_a)^{1/2}$ and $\Omega_a = eB_0/m_a c$ represent the plasma and cyclotron frequencies of species labeled as a, respectively; $\pm$ are adopted to differentiate the right-handed (RH) and left-handed (LH) circularly polarized electromagnetic modes, respectively; m_a is the mass of species of sort a; e, c, n_0, and B_0 stand for the unit electric charge, speed of light *in vacuo*, total number density, and intensity of the ambient magnetic field, respectively. A similar dispersion relation has already been employed by Lazar and Poedts[22] in order to quantify the role of non-thermal species. Lazar and Poedts[23] show an interplay of EFH instability with Weibel instability in solar and space plasmas for bi-maxwellian form of distribution, and Lazar *et al.*[43] consider the core-halo dual structure model of solar wind electrons.

For a homogeneous plasma immersed in a uniform static magnetic field and large extended system, the assumed distribution function for both species is a bi-Maxwellian form, which is presumed to represent the plasma state for all times

$$f_a = \frac{1}{\pi^{3/2}\alpha_{\perp a}^2(t)\alpha_{\parallel a}(t)}\exp\left(-\frac{v_\perp^2}{\alpha_{\perp a}^2(t)} - \frac{v_\parallel^2}{\alpha_{\parallel a}^2(t)}\right), \quad (3)$$

except that perpendicular and parallel temperatures may evolve in time t. In the above equation (3), $\alpha_{\perp a}$ and $\alpha_{\parallel a}$ stand for perpendicular and parallel thermal speeds of species labeled a, and are defined by

$$\begin{aligned} T_{\perp a} &= \frac{m_a}{2}\int d\mathbf{v} v_\perp^2 f_a = \frac{m_a \alpha_{\perp a}^2}{2}, \\ T_{\parallel a} &= m_a \int d\mathbf{v} v_\parallel^2 f_a = \frac{m_a \alpha_{\parallel a}^2}{2}, \end{aligned} \quad (4)$$

where the customary Boltzmann constant is omitted here by putting the dynamics of system in cgs unit for thermal energy. Particles possessing non-thermal velocities significantly deviate from the bi-Maxwellian form of distribution (3). Various authors such as Lazar and Poedts[22] and Vinas *et al.*[44] quantified the role of kappa index for unstable EFH mode in Earth's magnetospheres, space and solar wind plasmas. For the present study of slow solar wind in Heliospheric radial range, the observed value of kappa index is around 6 to 7 as reported by Maksimovic *et al.*[45] For these values of kappa parameter, the dispersion curves deviate insignificantly from the bi-Maxwellian case. Under these circumstances, the solar wind electrons can be best modeled by bi-Maxwellian distribution (3).

The assumed model distribution function (3) is an approximation which is not expected to be valid in a strict sense. In the nonlinear stage, the wave-particle interaction in time history leads to the distortion of the resonant velocity space, thereby the distribution is expected to deviate from its bi-Maxwellian form. For instance, in textbook gentle bump-on-tail instability, which involves a small portion of resonant velocity space, the same approximation cannot be blindly employed. In our case, where we are interested in the characteristic growth rate and range of unstable mode of an anisotropic driven instability, which are largely determined by bulk velocity moments, i.e., perpendicular and parallel temperatures (4), the assumption of self-similar form for particle distribution function may be valid at least in an approximate sense. In simulations, e.g., by Hellinger *et al.*,[30] it is shown that the electron distribution function indeed deviates from the bi-Maxwellian form. However, Ref. 30 plots the distribution function in only representative time steps. In contrast, in the comparative study between the macroscopic quasilinear theory and simulation of proton instabilities, Refs. 32–35 find that the deviation from bi-Maxwellian forms occurs as a transient feature, but over longer time intervals, quasi bi-Maxwellian forms are eventually restored. The more rigorous tests and validations are obviously called for, but for the present purpose, we adopt the bi-Maxwellian model as a first cut approach for the parallel electron firehose instability.

Employing the distribution function (3) in Equation (2), the complex frequency ω and wave number k of LH circularly polarized electromagnetic mode satisfies the following instantaneous dispersion relation

$$\begin{aligned} 0 = \frac{c^2k^2}{\omega_{pi}^2} - \frac{T_{\perp i}}{T_{\parallel i}} + 1 - \left[\frac{T_{\perp i}}{T_{\parallel i}}\omega - \left(\frac{T_{\perp i}}{T_{\parallel i}} - 1\right)\Omega_i\right] \\ \times \frac{1}{k\alpha_{\parallel i}} Z\left(\frac{\omega - \Omega_i}{k\alpha_{\parallel i}}\right) - \frac{m_i}{m_e}\left\{\frac{T_{\perp e}}{T_{\parallel e}} - 1\right. \\ \left. + \left[\frac{T_{\perp e}}{T_{\parallel e}}\omega + \left(\frac{T_{\perp e}}{T_{\parallel e}} - 1\right)\Omega_e\right]\frac{1}{k\alpha_{\parallel e}} Z\left(\frac{\omega + \Omega_e}{k\alpha_{\parallel e}}\right)\right\}. \end{aligned} \quad (5)$$

where we have ignored the displacement current. In Equation (5), the plasma dispersion function is defined by

$$Z(\zeta) = \int_{-\infty}^{\infty} \frac{e^{-x^2}dx}{x - \zeta}.$$

The above relation (5) adiabatically depends upon the time variable t through the temperatures of ions and electrons.

For the parallel waves and instabilities, the particle kinetic equation in the diffusion approximation is given by taking into account only the left-hand polarized mode (this is because the electron firehose instability corresponds to the left-hand mode)

$$\begin{aligned} \frac{\partial f_a}{\partial t} = \frac{ie^2}{4m_a^2c^2}\frac{1}{v_\perp}\int_{-\infty}^{\infty}\frac{dk}{k^2}\left[\left(\omega^* - kv_\parallel\right)\frac{\partial}{\partial v_\perp} + kv_\perp\frac{\partial}{\partial v_\parallel}\right] \\ \times \frac{v_\perp \delta B^2(k,\omega)}{\omega - kv_\parallel - \Omega_a}\left[\left(\omega - kv_\parallel\right)\frac{\partial f_a}{\partial v_\perp} + kv_\perp\frac{\partial f_a}{\partial v_\parallel}\right], \end{aligned} \quad (6)$$

where $\omega = \omega_k + \imath\gamma_k$ is the complex root of Equation (5), and $\delta B^2(k)$ is the spectral wave energy density associated with magnetic field perturbations. The rigorous quasilinear theory comprises of directly solving the particle kinetic Equation (6). However, in the present case, we take a simplifying approach of taking the macroscopic moments of the particle equation. The approach is named the macroscopic quasilinear theory, through which we are particularly interested in the time evolution of perpendicular and parallel temperatures. Dynamical equations for the temperatures are governed by the moments $m_a v_\perp^2/2$ and $m_a v_\parallel^2$ of Equation (6), respectively, as

$$\begin{aligned} \frac{dT_{\perp a}}{dt} = -\frac{e^2}{2m_ac^2}\int_{-\infty}^{\infty}\frac{dk}{k^2}\delta B^2(k)\left\{\left(\frac{2T_{\perp a}}{T_{\parallel a}} - 1\right)\gamma_k\right. \\ + \Im\frac{2i\gamma - (\pm)^\sigma\Omega_a}{k\alpha_{\parallel a}}\left[\frac{T_{\perp a}}{T_{\parallel a}}\omega - (\pm)^\sigma\left(\frac{T_{\perp a}}{T_{\parallel a}} - 1\right)\Omega_a\right] \\ \left.\times Z\left(\frac{\omega - (\pm)^\sigma\Omega_a}{k\alpha_{\parallel a}}\right)\right\}, \\ \frac{dT_{\parallel a}}{dt} = \frac{e^2}{m_ac^2}\int_{-\infty}^{\infty}\frac{dk}{k^2}\delta B^2(k)\left\{\frac{T_{\perp a}}{T_{\parallel a}}\gamma_k + \Im\frac{\omega - (\pm)^\sigma\Omega_a}{k\alpha_{\parallel a}}\right. \\ \left.\times\left[\frac{T_{\perp a}}{T_{\parallel a}}\omega - (\pm)^\sigma\left(\frac{T_{\perp a}}{T_{\parallel a}} - 1\right)\Omega_a\right]Z\left(\frac{\omega - (\pm)^\sigma\Omega_a}{k\alpha_{\parallel a}}\right)\right\}, \end{aligned} \quad (7)$$

where $\sigma = +1$ corresponds to ions and $\sigma = -1$ is for electrons species. Upon explicitly writing Eq. (7) for protons and electrons

$$\frac{dT_{\perp i}}{dt} = -\frac{e^2}{2m_i c^2}\int_{-\infty}^{\infty}\frac{dk}{k^2}\langle\delta B^2(k)\rangle\left\{\left(\frac{2T_{\perp i}}{T_{\|i}}-1\right)\gamma_k + \mathrm{Im}\,\frac{2i\gamma-\Omega_i}{k\alpha_{\|i}}\left[\frac{T_{\perp i}}{T_{\|i}}\omega-\left(\frac{T_{\perp i}}{T_{\|i}}-1\right)\Omega_i\right]Z\left(\frac{\omega-\Omega_i}{k\alpha_{\|i}}\right)\right\},$$
$$\frac{dT_{\|i}}{dt} = \frac{e^2}{m_i c^2}\int_{-\infty}^{\infty}\frac{dk}{k^2}\langle\delta B^2(k)\rangle\left\{\frac{T_{\perp i}}{T_{\|i}}\gamma_k + \mathrm{Im}\,\frac{\omega-\Omega_i}{k\alpha_{\|i}}\left[\frac{T_{\perp i}}{T_{\|i}}\omega-\left(\frac{T_{\perp i}}{T_{\|i}}-1\right)\Omega_i\right]Z\left(\frac{\omega-\Omega_i}{k\alpha_{\|i}}\right)\right\},$$
$$\frac{dT_{\perp e}}{dt} = -\frac{e^2}{2m_e c^2}\int_{-\infty}^{\infty}\frac{dk}{k^2}\langle\delta B^2(k)\rangle\left\{\left(\frac{2T_{\perp e}}{T_{\|e}}-1\right)\gamma_k + \mathrm{Im}\,\frac{2i\gamma+\Omega_e}{k\alpha_{\|e}}\left[\frac{T_{\perp e}}{T_{\|e}}\omega+\left(\frac{T_{\perp e}}{T_{\|e}}-1\right)\Omega_e\right]Z\left(\frac{\omega+\Omega_e}{k\alpha_{\|e}}\right)\right\},$$
$$\frac{dT_{\|e}}{dt} = \frac{e^2}{m_e c^2}\int_{-\infty}^{\infty}\frac{dk}{k^2}\langle\delta B^2(k)\rangle\left\{\frac{T_{\perp e}}{T_{\|e}}\gamma_k + \mathrm{Im}\,\frac{\omega+\Omega_e}{k\alpha_{\|e}}\left[\frac{T_{\perp e}}{T_{\|e}}\omega+\left(\frac{T_{\perp e}}{T_{\|e}}-1\right)\Omega_e\right]Z\left(\frac{\omega+\Omega_e}{k\alpha_{\|e}}\right)\right\}. \tag{8}$$

The wave kinetic equation is given by

$$\frac{\partial\delta B^2(k)}{\partial t} = 2\gamma_k\,\delta B^2(k). \tag{9}$$

For oblique propagations, we will have a different generalized dispersion relation (2) and particle kinetic Equation (6). Introducing the obliqueness in propagation would alter the growth rate of the unstable mode (first order analysis) and obviously, dynamical temperatures Equation (7), second order analysis, will be revised as well. So, for different propagations, different regimes, and having different instability thresholds, both (oblique and strictly parallel propagating) modes may have different conclusions. The oblique propagation of unstable propagating EFH mode may be taken as future task.

III. NUMERICAL ANALYSIS

For numerical analysis, we introduce the following dimensionless (or normalized) quantities

$$z=\frac{\omega}{\Omega_i},\quad q=\frac{ck}{\omega_{pi}}=\frac{kv_A}{\Omega_i},\quad \tau=\Omega_i t,\quad M=\frac{m_i}{m_e},$$
$$\beta_{\perp i}=\frac{8\pi n_0 T_{\perp i}}{B_0^2}=\frac{\alpha_{\perp i}^2}{v_A^2},\quad \beta_{\|i}=\frac{8\pi n_0 T_{\|i}}{B_0^2}=\frac{\alpha_{\|i}^2}{v_A^2},$$
$$\beta_{\perp e}=\frac{8\pi n_0 T_{\perp e}}{B_0^2}=\frac{\alpha_{\perp e}^2}{v_A^2}\frac{1}{M},\quad \beta_{\|e}=\frac{8\pi n_0 T_{\|e}}{B_0^2}=\frac{\alpha_{\|e}^2}{v_A^2}\frac{1}{M},$$
$$A_i=\frac{\beta_{\perp i}}{\beta_{\|i}}-1,\quad A_e=\frac{\beta_{\perp e}}{\beta_{\|e}}-1,$$
$$\zeta_i=\frac{z-1}{q\beta_{\|i}^{1/2}},\quad \zeta_e=\frac{z+M}{q\left(M\beta_{\|e}\right)^{1/2}},$$
$$\eta_i=\frac{(A_i+1)z-A_i}{q\beta_{\|i}^{1/2}},\quad \eta_e=\frac{M^{1/2}((A_e+1)z+MA_e)}{q\beta_{\|e}^{1/2}},$$
$$W(q)=\frac{\delta B^2(q)}{B_0^2}. \tag{10}$$

Let us rewrite Equations (5), (8), and (9), respectively, in normalized form as

$$0 = q^2 - A_i - MA_e - \eta_i Z(\zeta_i) - \eta_e Z(\zeta_e), \tag{11}$$

$$\frac{d\beta_{\perp e}}{d\tau} = -\int\frac{dq}{q^2}W(q)\left\{M(2A_e+1)z_i + \mathrm{Im}\,(2iz_i+M)\,\eta_e Z(\zeta_e)\right\},$$
$$\frac{d\beta_{\|e}}{d\tau} = 2\int\frac{dq}{q^2}W(q)\left\{M(A_e+1)z_i + \mathrm{Im}\,(z+M)\,\eta_e Z(\zeta_e)\right\},$$
$$\frac{d\beta_{\perp i}}{d\tau} = -\int\frac{dq}{q^2}W(q)\left\{(2A_i+1)z_i + \mathrm{Im}\,(2iz_i-1)\eta_i Z(\zeta_i)\right\},$$
$$\frac{d\beta_{\|i}}{d\tau} = 2\int\frac{dq}{q^2}W(q)\left\{(A_i+1)z_i + \mathrm{Im}\,(z-1)\eta_i Z(\zeta_i)\right\}. \tag{12}$$

$$\frac{\partial W(q)}{\partial\tau} = 2z_i W(q). \tag{13}$$

Equation (12) depicts the dynamical variation of parallel and perpendicular temperatures of ions and electrons via instantaneous dispersion relation (11) in each time step τ. For linear analysis, it may be appropriate to consider the isotropic ions,[22,23] but our numerical analyses show that the protons undergo a perpendicular heating and parallel cooling (or heating) in the nonlinear phase. As a consequence, isotropic ions are adopted as initial conditions, but in our quasilinear scheme, we allow the ions to evolve in time. In dynamical states of electron temperatures, particle-in-cell simulation results in 1D[27,28] and 2D[29,30] show that the ions are indeed affected by electron firehose (EFH) instability. Our aim is to provide a theoretical development of time evolution of temperatures along with wave energy density. Also, the marginal stability curve, which is represented by the inverse relationship (1), appears in saturation stages of our calculations, since it is built into the system by virtue of the assumption of bi-Maxwellian model. The present quasilinear treatment does not include higher-order nonlinear effects such as weak turbulence effects,[46–48] which is beyond the scope of the present study, but may be taken as future task.

Numerical solutions to Eq. (11) are displayed in Figure 1. For graphical analysis, the realistic value of parameter $\beta_{\|i}=0.04$ is adopted. The ions are assumed to be isotropic, $T_{\perp i}=T_{\|i}=T_i$. We consider the electron temperature ratio of $T_{\perp e}/T_{\|e}=0.1$ and take relatively a high parallel beta $\beta_{\|e}=3$. This is because the parallel electron firehose instability requires a high beta. Observations of electron temperature near 1 AU shows that sometimes solar wind electrons possess such high beta values.[49,50] Figure 1 depicts the variation of normalized frequency, $z_r=\omega_k/\Omega_i$, and growth rate, $z_i=\gamma_k/\Omega_i$, against normalized wavenumber, $q=ck/\omega_{pi}$, for different

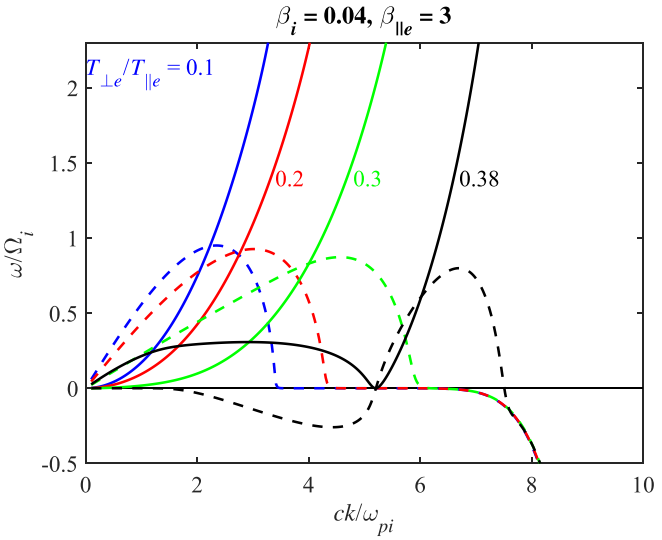

FIG. 1. Complex real frequency, ω_k/Ω_i (solid lines), and growth rate, γ_k/Ω_i (dotted), versus normalized wave number, ck/ω_{pi}, for different combinations of temperature ratios for electrons.

anisotropic ratios of the electrons. Note that the growth rate of EFH instability is suppressed by increasing the electron temperature ratios. For $T_{\perp e}/T_{\|e} = 0.1$, 0.2, and 0.3, the instability exists for a low k regime, but eventually, for a high k, the mode becomes heavily damped. For $T_{\perp e}/T_{\|e} = 0.38$ the quantity $z_i = \gamma_k/\Omega_i$ becomes negative (damping) for low k and the instability exists for intermediate k. For high k, the mode becomes heavily damped as in other cases.

Figure 2 displays the time history of variation in normalized temperatures (or betas) for electrons and protons, as well as the wave energy density. The initial conditions are chosen as various combinations of the following parameters:

$$\begin{aligned} &W(k) = 10^{-6}, \quad \beta_{\|i}(0) = 0.04, \\ &\frac{T_{\perp i}(0)}{T_{\|i}(0)} = \frac{\beta_{\perp i}(0)}{\beta_{\|i}(0)} = 1, \\ &\frac{T_{\perp e}(0)}{T_{\|e}(0)} = \frac{\beta_{\perp e}(0)}{\beta_{\|e}(0)} = 0.1, \\ &\beta_{\|e}(0) = 3,\ 4,\ 5. \end{aligned} \tag{14}$$

In all three cases, initial electron temperature ratio is taken to be $T_{\perp e}(0)/T_{\|e}(0) = \beta_{\perp e}(0)/\beta_{\|e}(0) = 0.1$. The left most panels correspond to the initial value of electron beta $\beta_{\|e}(0) = 3$; for middle panels, the initial value is $\beta_{\|e}(0) = 4$; for right hand panels, the same is $\beta_{\|e}(0) = 5$. The parallel EFH instability is excited by parallel electron temperature anisotropy, which is opposite to that of the electromagnetic electron cyclotron (EMEC) instability.[51,52] The method of analyzing the time evolution of anisotropy-driven instability by means of macroscopic quasilinear theory was pioneered by Ref. 53. Figure 2 shows that EFH instability leads to the reduction in the electron parallel temperature (or $\beta_{\|e}$) and an increase in the perpendicular temperature ($\beta_{\perp e}$), while concomitantly, it leads to the perpendicular heating of the protons (increase in $\beta_{\perp i}$). As for the parallel proton temperature, or $\beta_{\|i}$, the first case (left-hand panels) shows a parallel cooling of protons, but in the middle and right-hand panels, the protons are seen to undergo a slight parallel heating. Note that even though the protons develop the perpendicular

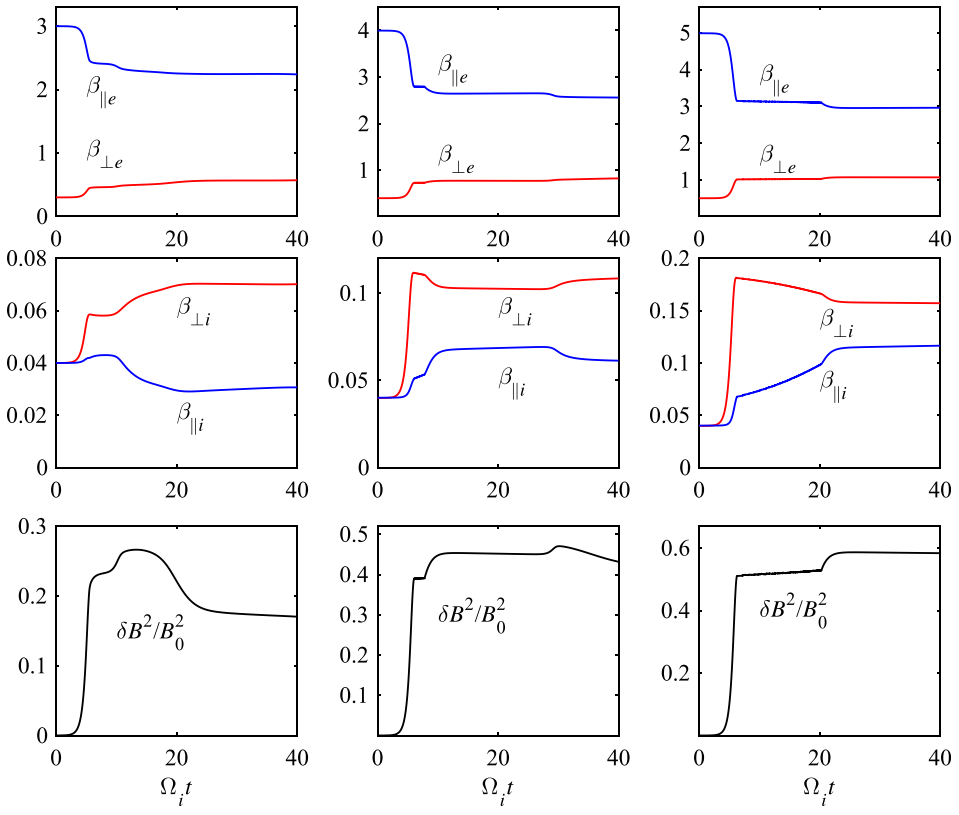

FIG. 2. Time evolution of normalized temperatures (betas) for electrons, $\beta_{\perp e}$ and $\beta_{\|e}$ (top), for protons, $\beta_{\perp i}$ and $\beta_{\|i}$ (middle), and wave energy density $\delta B^2/B_0^2$ (bottom), versus normalized time, $\tau = \Omega_i t$. All three cases correspond to the initial anisotropy $\beta_{\perp e}(0)/\beta_{\|e}(0) = 0.1$. Left-hand panels are for initial parameter $\beta_{\|e}(0) = 3$; the middle panels are for $\beta_{\|e}(0) = 4$, the right-hand panels represent the initial condition $\beta_{\|e}(0) = 5$.

temperature anisotropy, the change in the proton temperatures is quite small. In general, the free energy source for the instability resides in the initial excessive parallel electron temperature anisotropy. The perpendicular heating and parallel cooling of electrons leads to the stabilization of EFH instability the wave energy density increases exponentially, as dictated by the linearized Vlasov theory, but such an exponential rise in amplitude is arrested at saturation stages due to quasilinear relaxation mechanisms. Note that the saturation level of energy density becomes higher moving from left to right most panel due to larger magnitudes of initial parallel temperatures. It is also worth noting here that in the first case (left), the wave energy density first increases, saturates, but subsequently the level decreases again. The second (middle) and third (right) does not show this behavior. This dynamical variation in wave energy density is owing to the reabsorption of wave at different wave numbers at different time periods.

The elaboration of reabsorption mechanism of wave is presented in Figure 3. The left top and bottom panels show instantaneous dispersion relations at unit time interval $\Omega_i\Delta t = 1$ from the start until $\Omega_i t = 30$. Figure 3 corresponds to the first case, namely, the left panels in Figure 2. We have highlighted the time steps corresponding to $\Omega_i t = 0$, 5, 6, 10, and 20, using thicker lines and with different colors. Note that most rapid changes in the instantaneous dispersion relation occurs for time steps $\Omega_i t = 5$ and 6, and that for time interval between $\Omega_i t = 10$ and 30, there exists a range of low k space for which the mode is damped. This means that previously growing region of k space will now be damped. In other words, there exist a competition between the growing range of k space and damped region. It is interesting to see here that, in moving to longer time scales, growth rate is suppressed for small k and the ranges of peak growth rate moves to a higher k regime. For the sake of providing readers with better information, we also plot the wave spectrum as a function of k and time. The plot is shown in the right-hand panel. Note that high k wave spectrum is excited between $\Omega_i t = 10$ to 20 or so, but eventually subsides. The excitation of the high k branch is intimately related to the dynamic behavior of instantaneous growth/damping rate, as discussed above, namely, the appearance of low k damping region.

We repeat the instantaneous dispersion relation analysis and the dynamic spectral analysis in Figure 4, in the same format as in Figure 3. This is for second case shown in the middle panels of Figure 2. In this case, we highlight the time steps $\Omega_i t = 0$, 6, 21, and 30. The instantaneous dispersion relation curves for both real frequency and growth/damping rate are plotted for each time interval corresponding to $\Omega_i\Delta t = 1$, up to 40. The general trend of peak instability growth rate shifting to higher k remains the same, but the damped region associated with intermediate k only appears after $\Omega_i t = 21$ or so. For $\Omega_i t = 6$ until $\Omega_i t = 21$, the mode remains as damped mode, and the instability is re-excited only after $\Omega_i t = 21$ when the proton perpendicular temperature anisotropy has reached a certain critical level. This type of behavior could not have been predicted *a priori* on the basis of linear analysis. The time dependence of spectrum is shown on the right, in the same format as Figure 3. For the case shown in Figure 4, there is no high k secondary instability, and the wave spectrum is located in the same general unstable k range for all times. According to the instantaneous growth rate shown on the bottom-left panel, the instability is re-excited after $\Omega_i t = 21$ or so, with the peak growth rate located around $ck/\omega_{pi} \sim 6$. Upon a close examination of the wave intensity, there is in fact a minimal increase in the wave amplitude around $ck/\omega_{pi} \sim 6$ after the time period of $\Omega_i t > 21$, but the increase is only barely apparent in the

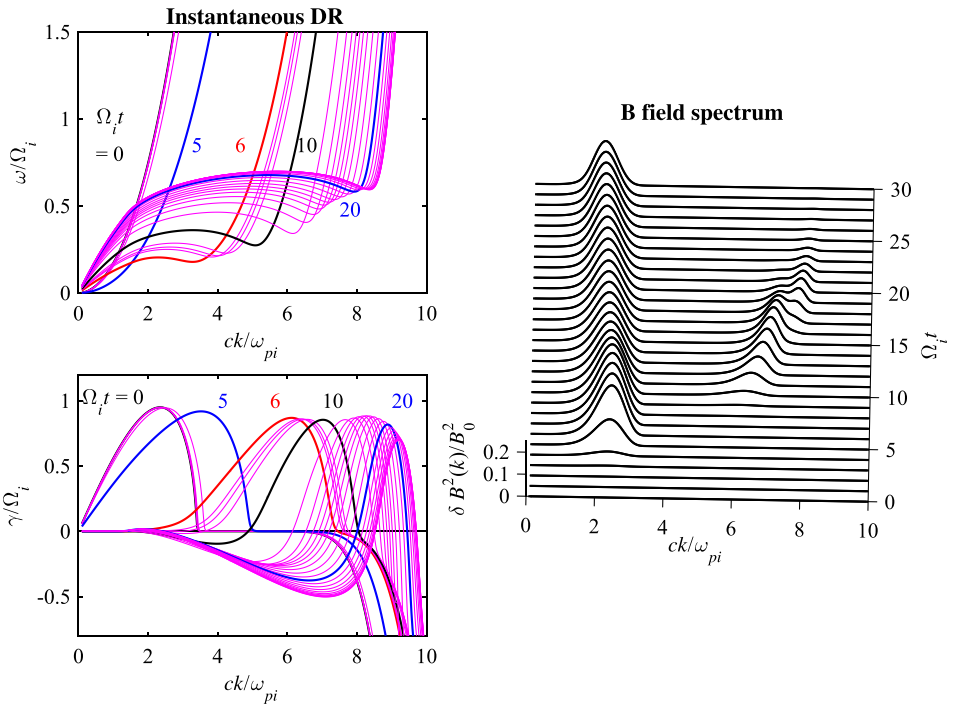

FIG. 3. Complex real frequency, $z_r = \omega_k/\Omega_i$ (top left), and growth rate, $z_i = \gamma_k/\Omega_i$ (bottom left), versus normalized wave number, $q = ck/\omega_{pi}$, for each interval of normalized time, $\Delta\tau = \Omega_i\Delta t = 1$, ranging from 0 to 30. We highlight Ω_t = 0, 6, 10, and 20. The right-hand panel shows the temporal behavior associated with the wave spectrum. This figure is for the first case shown in Figure 2, left panels.

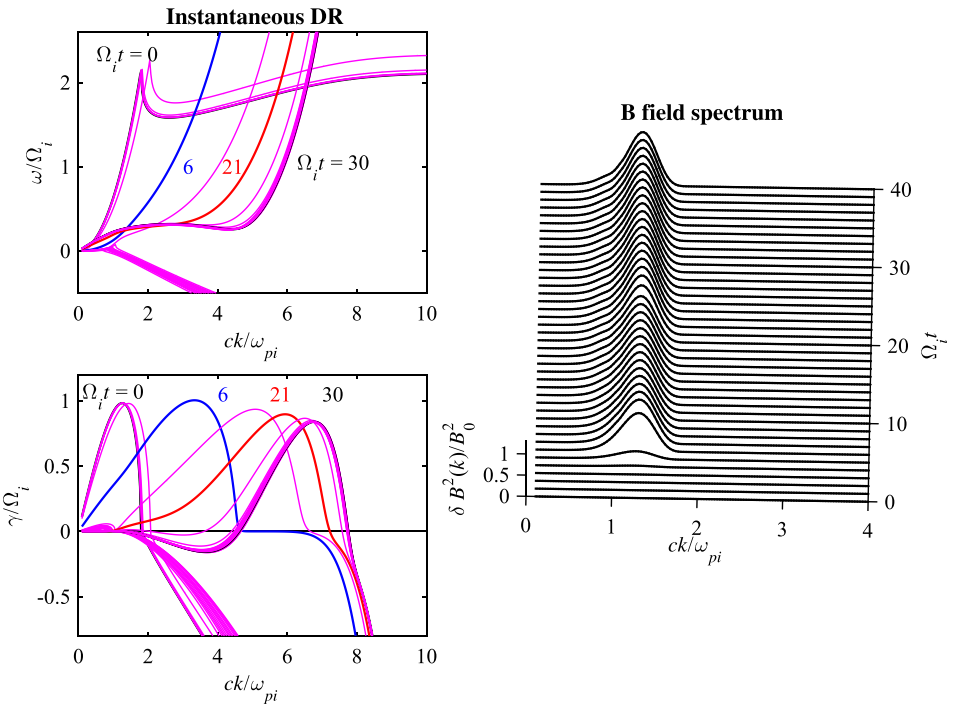

FIG. 4. The same format as Figure 3, except that this figure corresponds to the second case shown in the middle panels of Figure 2.

logarithmic scale. In the linear vertical scale used in the right-hand panel, such a minimal intensity becomes virtually invisible, so for the purpose of visualization, we limited the plotting range to $0 < ck/\omega_{pi} < 4$. To reiterate, the behavior associated with the wave spectrum could not have been predicted *a priori*.

Figure 5 displays numerical solutions in which the initial conditions are

$$\begin{aligned} &W(k) = 10^{-6}, \quad \beta_{\|i}(0) = 0.04, \\ &\frac{T_{\perp i}(0)}{T_{\|i}(0)} = \frac{\beta_{\perp i}(0)}{\beta_{\|i}(0)} = 1, \\ &\frac{T_{\perp e}(0)}{T_{\|e}(0)} = \frac{\beta_{\perp e}(0)}{\beta_{\|e}(0)} = 0.15,\ 0.25,\ 0.35, \\ &\beta_{\|e}(0) = 4. \end{aligned} \tag{15}$$

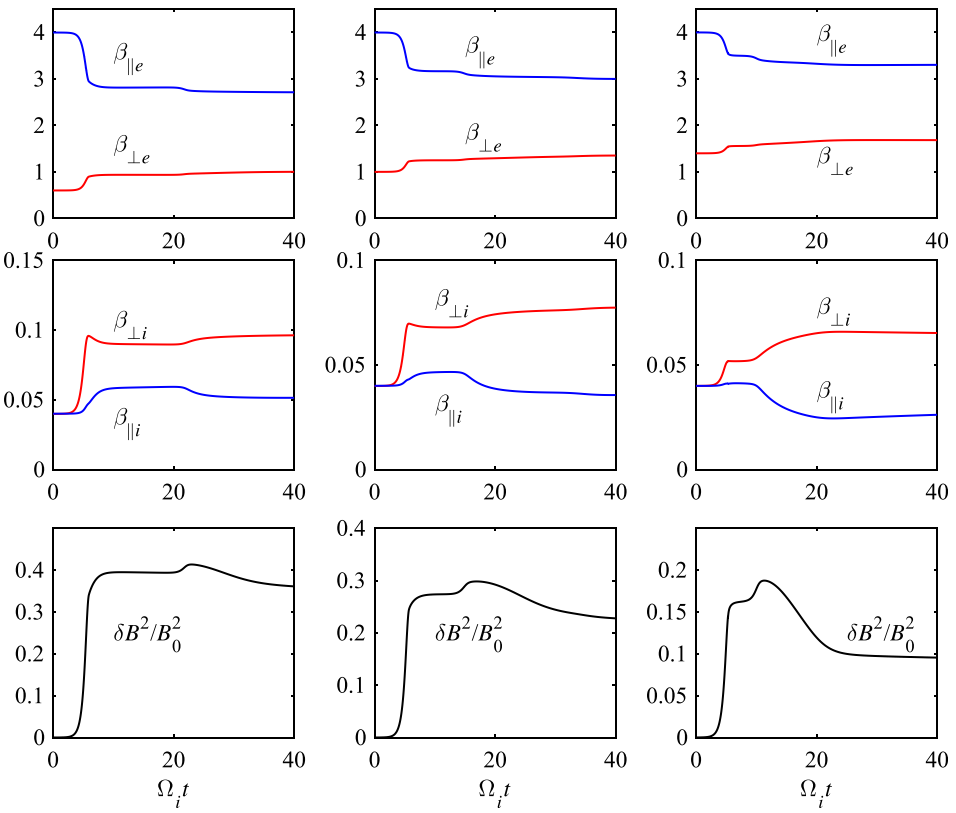

FIG. 5. The same as Figure 2, except that we consider an initial parameter $\beta_{\|e}(0) = 4$ for all three cases. Left-hand panels are for $\beta_{\perp e}(0)/\beta_{\|e}(0) = 0.15$; the middle panels are for $\beta_{\perp e}(0)/\beta_{\|e}(0) = 0.25$; the right-hand panels represent the initial condition $\beta_{\perp e}(0)/\beta_{\|e}(0) = 0.35$.

For Figure 5, the initial electron beta value $\beta_{\parallel e}(0) = 4$ is same for all panels. The left-most panels are for an initial value of electron temperature ratio $\beta_{\perp e}(0)/\beta_{\parallel e}(0) = 0.15$; the initial condition for middle panels corresponds to $\beta_{\perp e}(0)/\beta_{\parallel e}(0) = 0.25$; the right-hand panels are for $\beta_{\perp e}(0)/\beta_{\parallel e}(0) = 0.35$. As in Figure 2, as time progresses, the free energy associated with electron temperature anisotropy is reduced through increase in perpendicular beta and reduction in parallel beta. As far as the protons are concerned, initially isotropic protons generally attain a perpendicular anisotropy via perpendicular heating, but the parallel temperature shows a complex behavior. For the left- and middle panels, the parallel proton temperature first undergoes an increase, followed by a decrease, but the asymptotic value does not change much from the initial value. In contrast, for the right-hand panel, the protons undergo a general parallel cooling. The wave energy density undergoes an exponential increase, followed by saturation, but beyond saturation, there exists a small hump, which subsequently decreases. The decrease is most prominent for the right-most panel, which resembles the left-most panel of Figure 2. In order to avoid repetition, we do not show an instantaneous dispersion relation analysis nor the time evolution of wave spectrum for any cases shown in Figure 5.

To summarize our findings, in Figure 6, we re-plot the results shown in Figures 2 and 5 in a different way. We combine all six cases into a single plot by following the dynamic paths of electrons and protons. We display the electron temperatures as paths in $(\beta_{\parallel e}, T_{\perp e}/T_{\parallel e})$ phase space, and we also color code the strength of magnetic field using the color scale. We do the same for protons in $(\beta_{\parallel i}, T_{\perp i}/T_{\parallel i})$ phase space, but since the two charged particle species overlap, we omit the species labels in the axes. Instead, we indicate the protons and electrons within the figure. Figure 6 depicts the particle and as well as field information for all six cases

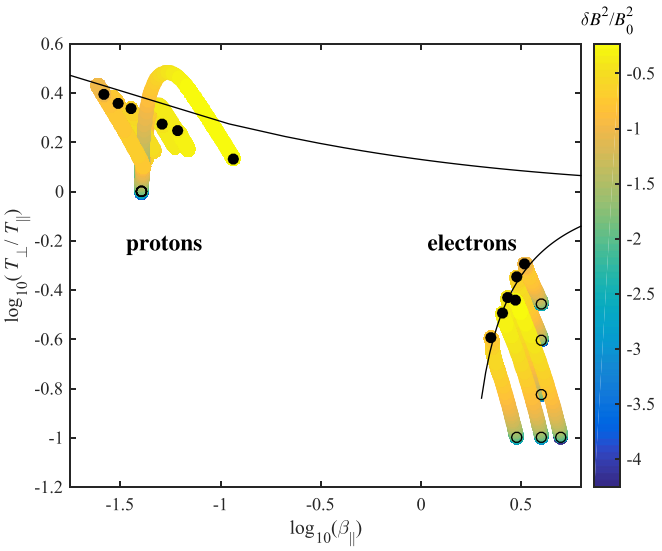

FIG. 6. The trajectories of the "solar wind" in $(\beta_\parallel, T_\perp/T_\parallel)$ space for both protons and electrons, whose initial conditions for all six cases considered in Figures 2 and 5 are shown with open circles. Final positions are marked with large dots and the wave energy density is depicted in terms of the color level. We also superposed the heuristic marginal stability curve following Lazar *et al.*[24] and Hellinger *et al.*[54]

considered so far. We also superpose the empirical marginal stability curve fitted with parameters given in Table 2 of Ref. 24 for parallel EFH instability, namely

$$\frac{T_{\perp e}}{T_{\parallel e}} = 1 - \frac{1.70}{\beta_{\parallel e}^{0.99}}, \tag{16}$$

and for proton cyclotron marginal stability curve as suggested by Hellinger *et al.*,[54] that is

$$\frac{T_{\perp i}}{T_{\parallel i}} = 1 + \frac{0.35}{\beta_{\parallel i}^{0.42}}. \tag{17}$$

It is worth mentioning here that, as time progresses, all trajectories corresponding to different initial conditions march to the marginal stability curve. For electrons, initially unstable states all end up near the marginal parallel electron firehose threshold curve (16), while the initially isotropic protons are heated in a perpendicular direction. Note that when the protons exceed the electromagnetic proton-cyclotron marginal instability condition, then they are expected to excite the left-hand proton cyclotron instability. In fact, the present formalism automatically contains the proton-cyclotron instability. Consider Fig. 3 left-hand panels, for instance. At $\Omega_i t = 0$, the real frequency and growth rate feature the classic electron firehose instability characteristics. However, as time proceeds, to say, $\Omega_i t = 6$, then the real frequency begins to exhibit characteristics of both EFH mode (with increasing frequency for large k) as well as the proton-cyclotron mode (that is, the flat part of the wave dispersion relation around $ck/\omega_{pi} \sim 2$ or so). The mode really takes on the characteristics of proton-cyclotron wave for $\Omega_i t = 20$, although there, the proton-cyclotron part of the mode is damped while the firehose mode part of the real frequency is associated with the growth rate. The point is that the left-hand electron firehose mode is really a combination of proton-cyclotron and firehose modes. In any event, eventually, all of the proton ensembles line up near the marginal proton-cyclotron marginal stability threshold condition (17). This is not too surprising since the present macroscopic quasilinear formalism inherently contains the anisotropy-beta inverse relationship such that the empirical fitting is automatically reproduced at the end of each quasilinear calculation. However, the nonlinear (or quasilinear, to be more precise) behavior of initially isotropic protons undergoing perpendicular heating, could not have been predicted *a priori* solely based upon the linear theory. Moreover, the timescale of the instability saturation or the asymptotic wave energy density could not be estimated accurately on the basis of the linear theory. Among the present findings, the interplay of electron and protons appears to be most interesting and relevant to solar wind dynamics, since the present study reveals that the electron firehose instability is capable of dynamically coupling the protons and electrons. The present finding also shows that the present macroscopic quasilinear formalism, if it can be verified by means of more rigorous simulations and more importantly, if the formalism can be extended to include oblique modes, may eventually be incorporated into the global-kinetic model of the solar wind of various types discussed in the literature.[31,39–41]

IV. SUMMARY AND DISCUSSION

The solar wind as a turbulence laboratory[55] receives attentions from scientists for many years. In the radially expanding plasma, the electron distribution becomes skewed due to the easily developed heat flux.[22] The CGL (Chew-Goldberger-Low) relations[56] predict the variation of temperature anisotropy and plasma beta following the scaling as $T_{\perp e}/T_{\|e}$, $\beta_{\|e} \propto r^{-2}$. According to *in situ* measurements, such as done by Ulysses spacecraft near 1 AU, the observed values of anisotropies are not in agreement with CGL predictions. Besides, it should be noted that the CGL approximation is not strictly applicable for electrons in the solar wind anyway. The electron distribution function exhibits strong heat fluxes that invalidate the CGL approach based upon the quasi-Maxwellian distribution function. It is noted that, different plasma micro-instabilities are contributing to regulate and limit the upper limits of anisotropies. The electron firehose instability is operative for excessive parallel thermal spread along the ambient magnetic field (i.e., $T_{\|e} > T_{\perp e}$), thereby put constraints on parallel electron temperature anisotropy to provide the required criteria for further acceleration.[27]

In the literature, linearized Vlasov theory and simulations have been applied to discuss the growth rates of EFH instability along with its empirically constructed marginal stability curve. For the first time, we adopted a theoretical quasilinear approach to display the time asymptotic states of electron temperature anisotropies and parallel plasma betas along with its wave energy density. We have also considered the dynamic response of protons to the excitation of parallel electron firehose instability. We assumed the bi-Maxwellian form of distribution for all times, except that perpendicular and parallel temperatures (defined in equation (4)) may vary in time t. In a strict sense, it is not a general approach, but we believe that it is valid as a simplest approximation, for the purpose of elaborating the phenomenon based on the bulk properties of the system, i.e., moments of the assumed distribution function. Many theoretical[31,35–38,51] and simulation results[32–34] support the same approximation, at least as a first cut approach.

Figures 2 and 5 detail the variation of electron temperature anisotropies, electron parallel betas, and wave energy density explicitly in time t for different combinations of initial conditions. In the time development, the excitation of parallel EFH mode leads to the regulation on the upper bound of parallel thermal spread through parallel cooling and perpendicular heating of electrons. The instability also leads to the perpendicular heating of the protons. Such an interplay between the electrons and protons may be important for solar wind dynamics, as the present parallel firehose instability dynamically couples the two charged particle species. The dynamical behavior of the wave energy density in time shows complex behaviors. The phenomenon of reabsorption of waves or lack thereof is displayed in Figures 3 and 4. In Figure 6, we re-plot all previous results and show the time history of all initial conditions (Figures 2 and 5). It is shown that initially unstable electron states all move towards the empirical marginal stability curve associated with the parallel EFI, while initially the isotropic protons all get heated in a perpendicular direction, and end up in the close vicinity of the proton cyclotron marginal states. In this way, it is shown that the electron firehose instability dynamically couples the protons and electrons.

To reiterate, our quasilinear approach for parallel EFH instability provides the sense of how fast the instability attains the saturation stage. It is shown that, via same approach, one can compute the saturated magnetic field intensity level as a function of the electron temperature ratios and parallel betas. Our findings may also be helpful in view of the NASA's upcoming Solar Probe Plus mission and ESA's Solar Orbiter mission. The present theoretical approach and modeling may benefit the space physics community. Next, we may extend this methodology for inhomogeneous (ambient magnetic field and density profiles) plasmas to display an interplay between electromagnetic electron cyclotron (EMEC) and electron fire hose (EFH) instabilities as a function of radial distance for the expanding solar wind. Such an approach amounts to global-kinetic solar wind modeling, which had been hitherto limited to the proton dynamics,[31,39–41] but now involving both electrons and protons.

Further, the instabilities excited in two (or three) dimensional space such as oblique fire hose[26,28] should be considered within the present macroscopic quasilinear framework. The inclusion of oblique electron firehose instability is of particular importance, since earlier studies by Li and Habbal[26] and Gary and Nishimura[28] established that the oblique firehose mode can have a much higher growth rate. This implies that in the early phase of the instability development, oblique firehose mode – or "resonant" firehose mode, according to Gary and Nishimura[28]—may completely dominate the dynamics. In this sense, including the oblique mode may fundamentally alter the conclusion reached in the present investigation. However, this problem must be regarded as a future research task since it is clearly beyond the scope of the present paper. Finally, as we assumed a simple distribution, a comparison between theory and full particle-in-cell simulation for EFH instability must also be done in order to not only verify and test the assumption of bi-Maxwellian distribution, but also to check to what extent the quasilinear theory is valid or not. These are all tasks for future research.

ACKNOWLEDGMENTS

The present paper does not involve any spacecraft data analysis. However, upon request, numerical data for generating all the figures will be made available. M.S. and S.S. acknowledge the support from Higher Education Commission (HEC), Pakistan. P.H.Y. acknowledges the NSF Grant No. AGS1550566 to the University of Maryland, and the BK21 plus program from the National Research Foundation (NRF), Korea, to Kyung Hee University. He also acknowledges the Science Award Grant from the GFT, Inc., to the University of Maryland.

[1]E. N. Parker, Astrophys. J. **128**, 664 (1958).
[2]J. W. Chamberlain, Astrophys. J. **133**, 675 (1961).
[3]K. Jockers, Astron. Astrophys. **6**, 219 (1970); available at http://articles.adsabs.harvard.edu/full/seri/A%2BA../0006/0000219.000.html.
[4]J. Lemaire and M. Scherer, J. Geophys. Res. **76**, 7479, doi:10.1029/JA076i031p07479 (1971).

[5]W. C. Feldman, B. L. Barraclough, J. T. Gosling, D. J. McComas, P. Riley, B. E. Goldstein, and A. Balogh, J. Geophys. Res. **103**, 14547, doi:10.1029/98JA00963 (1998).
[6]A. C. Fabian, Astron. Astrophys. **32**, 277 (1994).
[7]E. Marsch, in *Physics of the Inner Heliosphere II, Particles, Waves, and Turbulence*, edited by R. Schwenn and E. Marsch (Springer-Verlag, New York, 1991).
[8]E. E. Scime, S. J. Bame, W. C. Feldman, S. P. Gary, J. L. Phillips, and A. Balogh, J. Geophys. Res. **99**, 23401, doi:10.1029/94JA02068 (1994).
[9]S. J. Bame, D. J. McComas, B. L. Barraclough, J. L. Phillips, K. J. Sofaly, J. C. Chavez, B. E. Goldstein, and R. K. Sakurai, Astron. Astrophys. Suppl. Ser. **92**, 237 (1992); available at http://cdsads.u-strasbg.fr/cgi-bin/nph-iarticle_query?1992A%26AS...92..237B&data_type=PDF_HIGH&whole_paper=YES&type=PRINTER&filetype=.pdf.
[10]S. J. Schwartz, Rev. Geophys. **18**, 313, doi:10.1029/RG018i001p00313 (1980).
[11]D. A. Gurnett, in *Physics of the Inner Heliosphere II, Particles, Waves and Turbulence*, edited by R. Schwenn and E. Marsch (Springer-Verlag, New York, 1991), p. 135.
[12]S. P. Gary, *Theory of Space Plasma Microinstabilities* (Cambridge University Press, New York, 1993), and references therein.
[13]W. Manheimer and J. P. Boris, Plasma Phys. Fusion Technology **3**, 15 (1977).
[14]B. J. Anderson, S. A. Fuselier, S. P. Gary, and R. E. Denton, J. Geophys. Res. **99**, 5877, doi:10.1029/93JA02827 (1994).
[15]S. P. Gary, E. E. Scime, J. L. Phillips, and W. C. Feldman, J. Geophys. Res. **99**, 23391, doi:10.1029/94JA02067 (1994).
[16]J. V. Hollweg and H. J. Völk, Nature **225**, 441 (1970).
[17]J. V. Hollweg and H. J. Völk, J. Geophys. Res. **75**, 5297, doi:10.1029/JA075i028p05297 (1970).
[18]W. Pilipp and H. J. Völk, J. Plasma Phys. **6**, 1 (1971).
[19]W. Pilipp and A. O. Benz, Astron. Astrophys. **56**, 39 (1977); available at http://cdsads.u-strasbg.fr/cgi-bin/nph-iarticle_query?1977A%26A....56...39P&data_type=PDF_HIGH&whole_paper=YES&type=PRINTER&filetype=.pdf.
[20]S. P. Gary and C. D. Madland, J. Geophys. Res. **90**, 7607, doi:10.1029/JA090iA08p07607 (1985).
[21]J. V. Hollweg, J. Geophys. Res. **79**, 3845, doi:10.1029/JA079i025p03845 (1974).
[22]M. Lazar and S. Poedts, Astron. Astrophys. **494**, 311 (2009).
[23]M. Lazar and S. Poedts, Solar Phys. **258**, 119 (2009).
[24]M. Lazar, S. Poedts, R. Schlickeiser, and D. Ibscher, Sol. Phys. **289**, 369 (2014).
[25]G. Paesold and A. O. Benz, Astron. Astrophys. **351**, 741 (1999); available at http://cdsads.u-strasbg.fr/cgi-bin/nph-iarticle_query?1999A%26A...351..741P&data_type=PDF_HIGH&whole_paper=YES&type=PRINTER&filetype=.pdf.
[26]X. Li and S. R. Habbal, J. Geophys. Res. **105**, 27377, doi:10.1029/2000JA000063 (2000).
[27]P. Messmer, Astron. Astrophys. **382**, 301 (2002).
[28]S. P. Gary and K. Nishimura, Phys. Plasmas **10**, 3571 (2003).
[29]E. Camporeale and D. Burgess, J. Geophys. Res. **113**, A07107, doi:10.1029/2008JA013043 (2008).
[30]P. Hellinger, P. M. Trávníček, V. K. Decyk, and D. Schriver, J. Geophys. Res. **119**, 59, doi:10.1002/2013JA019227 (2014).
[31]P. H. Yoon and J. J. Seough, J. Geophys. Res. **119**, 7108, doi:10.1002/2014JA020261 (2014).
[32]J. J. Seough, P. H. Yoon, and J. Hwang, Phys. Plasmas **21**, 062118 (2014).
[33]J. J. Seough, P. H. Yoon, and J. Hwang, Phys. Plasmas **22**, 012303 (2015).
[34]J. J. Seough, P. H. Yoon, J. Hwang, and Y. Nariyuki, Phys. Plasmas **22**, 082122 (2015).
[35]P. H. Yoon, J. J. Seough, J. Hwang, and Y. Nariyuki, J. Geophys. Res. **120**, 6071, doi:10.1002/2015JA021495 (2015).
[36]J. J. Seough and P. H. Yoon, J. Geophys. Res. **117**, A08101, doi:10.1029/2012JA017645 (2012).
[37]P. H. Yoon and J. J. Seough, J. Geophys. Res. **117**, A08102, doi:10.1029/2012JA017697 (2012).
[38]J. J. Seough, P. H. Yoon, K.-H. Kim, and D. H. Lee, Phys. Rev. Lett. **110**, 071103 (2013).
[39]R. E. Denton, B. J. Anderson, S. P. Gary, and S. A. Fuselier, J. Geophys. Res. **99**, 11225, doi:10.1029/94JA00272 (1994).
[40]P. Hellinger and P. M. Trávníček, J. Geophys. Res. **113**, A10109, doi:10.1029/2008JA013416 (2008).
[41]B. D. G. Chandran, T. J. Dennis, E. Quataert, and S. D. Bale, Astrophys. J. **734**, 197 (2011).
[42]R. Schlickeiser, *Cosmic Ray Astrophysics* (Springer, Berlin, 2002).
[43]M. Lazar, S. M. Shaaban, S. Poedts, and Š. Štverák, MNRAS **464**, 564 (2017).
[44]A. F. Viñas, P. S. Moya, R. E. Navarro, J. A. Valdivia, J. A. Araneda, and V. Muñoz, J. Geophys. Res. **120**, 3307, doi:10.1002/2014JA020554 (2015).
[45]M. Maksimovic, I. Zouganelis, J.-Y. Chaufray, K. Issautier, E. E. Scime, J. E. Littleton, E. Marsch, D. J. McComas, C. Salem, R. P. Lin, and H. Elliott, J. Geophys. Res. **110**, A09104, doi:10.1029/2005JA011119 (2005).
[46]P. H. Yoon, Phys. Plasmas **22**, 082309 (2015).
[47]P. H. Yoon, Phys. Plasmas **22**, 092307 (2015).
[48]P. H. Yoon, Phys. Plasmas **22**, 082310 (2015).
[49]Š. Štverák, P. Trávníček, M. Maksimovic, E. Marsch, A. N. Fazakerley, and E. E. Scime, J. Geophys. Res. **113**, A03103, doi:10.1029/2007JA012733 (2008).
[50]M. L. Adrian, A. F. Vinas, P. S. Moya, and D. E. Wendel, Astrophys. J. **833**, 1 (2016).
[51]P. H. Yoon, J. J. Seough, K. H. Kim, and D. H. Lee, J. Plasma Phys. **78**, 47 (2012).
[52]M. Sarfraz, S. Saeed, P. H. Yoon, G. Abbas, and H. A. Shah, J. Geophys. Res. **121**, 9356, doi:10.1002/2016JA022854 (2016).
[53]R. C. Davidson and J. M. Ogden, Phys. Fluids **18**, 1045 (1975).
[54]P. Hellinger, P. Trávníček, J. C. Kasper, and A. J. Lazarus, Geophys. Res. Lett. **33**, L09101, doi:10.1029/2006GL025925 (2006).
[55]R. Bruno and V. Carbone, Living Rev. Sol. Phys. **10**, 2 (2013).
[56]G. F. Chew, M. L. Goldberger, and F. E. Low, Proc. R. Soc. London, Ser. A **236**, 112 (1956).